RSC Advances

PAPER

View Article Online
View Journal | View Issue

Cite this: *RSC Adv.*, 2022, **12**, 14439

Functionalized thiazolidone-decorated lanthanum-doped copper oxide: novel heterocyclic sea sponge morphology for the efficient detection of dopamine†

Umay Amara,[ab] Khalid Mahmood,[*a] Maria Hassan,[a] Muhammad Hanif,[c] Muhammad Khalid,[e] Muhammad Usman,[d] Zahid Shafiq,[a] Usman Latif,[b] Muhammad Mahboob Ahmed,[a] Akhtar Hayat[b] and Mian Hasnain Nawaz[*b]

Herein, we synthesized lanthanum (La)-doped sea sponge-shaped copper oxide (CuO) nanoparticles and wrapped them with novel O-, N- and S-rich (2*Z*,5*Z*)-3-acetyl-2-((3,4-dimethylphenyl)imino)-5-(2-oxoindolin-3-ylidene)thiazolidin-4-one (La@CuO-DMT). The shape and composition of the designed materials were confirmed by scanning electron microscopy (SEM), Fourier transform infrared (FTIR) spectroscopy, X-ray diffraction (XRD), and Raman spectroscopy. The graphitic pencil electrode (GPE) fabricated using La@CuO-DMT showed excellent sensing efficacy against dopamine (DA) with good selectivity, reproducibility and ideal stability. The unique morphology and massive surface defects by La@CuO offer good accessibility to DA and enhance smooth and robust channeling of electrons at the electrode–electrolyte interface. Consequently, these properties resulted in improved reaction kinetics and robust DA oxidation with an amplified faradaic response. Meanwhile, O-, N-, and S-enriched carbon support, *i.e.* DMT, inhibited the leaching of electrode matrixes, resulting in a superior detection limit of 423 nm and an improved sensitivity of 13.9 μA μM^{-1} cm^{-2} in the linear range of 10 μM to 1500 μM. Additionally, the developed sensing interface was successfully employed to analyze DA from tear samples with excellent percentage recoveries. We expect that such engineered morphology-based nanoparticles with a O-, N-, and S-rich C support will facilitate the development of DA sensors for *in vitro* screening of rarely studied tear samples with good sensitivity and selectivity.

Received 3rd March 2022
Accepted 24th April 2022

DOI: 10.1039/d2ra01406h

rsc.li/rsc-advances

1. Introduction

Dopamine (DA) is a classical neurotransmitter involved in the modulation of a multitude of neurological activities such as happiness, cognition, motivation, memory and fine motor control. DA dysfunction has been implicated in the pathogenesis of several neuronal disorders, primarily Parkinson's disease, neurodegeneration, schizophrenia, and traumatic stress disorders.[1–3] Therefore, DA homeostasis is the emblem of ongoing neurological health and physiological conditions. Many techniques have been exploited for the active monitoring of DA but electrochemical analysis provides a portable, economically viable assay platform with good quantitative readouts.[4–6] However, the poor selectivity owing to the coexisting species with comparable oxidizing potentials is the major challenge associated with the development of electrochemical DA sensors.[7] Meanwhile, electro-polymerization leading to electrode fouling and decreased intrinsic transduction response is also a great concern.[8] Therefore, DA diagnostics require the development of a cheap, sensitive and mechanically stable sensing interface that selectively output DA signals.

In these lines, scientists have exploited a plethora of nanomaterials, whilst nanostructures with a well-defined morphology were proved to enhance the sensitivity of the sensing interface.[9,10] In this regard, economically feasible copper oxide (CuO) with defined shape and highly reactive surface morphology has gained great interest.[11,12] Its smaller particle size, high surface-to-volume ratio, ideal stability in a variety of solutions and enhanced charge transfer capability

[a]*Institute of Chemical Sciences, Bahauddin Zakariya University, Multan 60800, Pakistan. E-mail: khalidmahmood@bzu.edu.pk*

[b]*Interdisciplinary Research Centre in Biomedical Materials (IRCBM), COMSATS University Islamabad, Lahore Campus, 54000, Pakistan. E-mail: mhnawaz@cuilahore.edu.pk*

[c]*Department of Pharmaceutics, Faculty of Pharmacy, Bahauddin Zakariya University, Multan, 608000, Pakistan*

[d]*Institute of Biomedical Materials and Engineering, College of Materials Science and Engineering, Qingdao University, 308 Ningxia Road, Qingdao, Shangdong 266071, China*

[e]*Department of Chemistry, Khwaja Fareed University of Engineering & Information Technology, Rahim Yar Khan, 64200, Pakistan*

† Electronic supplementary information (ESI) available. See https://doi.org/10.1039/d2ra01406h

lead to high redox activity.[13–15] Similarly, massive active sites, plentiful oxygen vacancies and good biocompatibility make it a potential sensing interface to specifically attract positively charged DA.[16,17] However, inherent shortcomings such as re-aggregation, Ostwald ripening and dissolution of CuO decrease the shelf life and eventually lead to poor electrode stability.[18,19]

Doping transition metal nanoparticles with rare earth element lanthanum (La) circumvents the aforementioned challenges and enhances the electrochemical properties of CuO. La as a dopant material has numerous remunerations such as low toxicity, thermal conductivity and excellent chemical stability that prevents CuO agglomeration and improves electrode life span and stability.[20,21] Moreover, La doping affects the structural traits owing to the large ionic radius of La^{3+} and can be easily added into the crystalline framework of CuO to acquire a unique nanostructure with various morphologies and ameliorated catalytic characteristics for sensing applications.[22] Significantly, La-coated probes have been employed as implantable sensors due to surface basicity, reduced oxide leakage and higher electron transfer kinetics,[23] which lead to an amplified transduction signal. However, it is still very challenging to fabricate a CuO-based stable transducing interface with lower detection limits and a higher faradaic response.

Fortunately, CuO tends to form hybrids with carbon (C)-containing organic moieties for the integration of highly stable,[24] electroactive interfaces with good selectivity and lower detection limits.[25] Nevertheless, the intrinsic charge carrier densities of carbon-based species are greatly dependent on their nitrogen content. Therefore, it is likely to exploit those sources that provide high nitrogen content besides carbon. In this respect, thiazolidone and its derivatives are the privileged core of N-, S- and O-containing bioactive heterocycles and have been extensively exploited as a scaffold for biological activities, drug development and fluorescent sensors.[26–28] They tend to interact with transition metals with different structural patterns owing to the presence of S, O and N and have the possibility to develop supra-molecular infrastructures with ideal stability that made them the ultimate choice for sensing usage.[29,30] However, still there is great room to further improve their intrinsic features such as charge carrier density and electrical conductivity by enhancing S and N contents.

In this work, we designed novel (2*Z*,5*Z*)-3-acetyl-2-((3,4-dimethylphenyl)imino)-5-(2-oxoindolin-3-ylidene)thiazolidin-4-one (DMT) as a source of O-, N-, and S-enriched graphitic carbon to decorate sea sponge-shaped La-doped CuO nanoparticles. This hybridization of La-doped CuO with DMT (La@CuO-DMT) endowed the integrated interface with high graphitic carbon content along with massive edge plane defects. The inter-vesicle spacing in the designed network results in robust tunneling of ions and electrons at the electrode–electrolyte interphase, leading to amplified faradaic response with a lower detection limit. Additionally, before the fabrication of La@CuO-DMT, we have also evaluated the response of CuO before and after doping with La against DA. The fabricated interface was eventually tested for tear sample evaluation against the analyte of interest, as part of real sample analysis for potential real-life applications.

2. Experimental section

2.1. Synthesis of copper oxide (CuO) and lanthanum-doped copper oxide (La@CuO) nanoparticles

CuO nanoparticles were prepared *via* a simple co-precipitation technique.[21] Briefly, copper(II) nitrate trihydrate (1 M) was dissolved in 100 mL distilled water and stirred for 30 minutes followed by the drop-wise addition of aqueous sodium hydroxide to attain pH 14. The pH was measured using a pH meter. The solution was subsequently heated at 80 °C and stirred for 30 minutes. The as-obtained mixture was centrifuged, washed with double distilled water and ethanol to remove impurities and dried at 50 °C for 48 hours. Meanwhile, the dried powder was thermally treated at 850 °C in a muffle furnace for 3 h. The same synthetic procedure was followed for the preparation of La-doped CuO by adding lanthanum nitrate hexahydrate (0.1 M) to the primary mixture, as shown in Scheme 1. The yield of the product was 87% and the product was synthesized in 3 repeated batches, which gave the same morphology as envisioned from SEM, indicating the good repeatability of the target product.

2.2. Synthesis of (2*Z*,5*Z*)-3-acetyl-2-((3,4-dimethylphenyl)imino)-5-(2-oxoindolin-3-ylidene)thiazolidin-4-one (DMT)

The novel isatin–thiazolidinone conjugate was prepared by the method reported by Naggar *et al.* with slight modifications.[31] Briefly, 2 mM isatin, bromoacetic acid, *N*,*N*′-aryl-acyl thiourea, bromoacetic acid and 4 mM sodium acetate as catalysts were refluxed for 4 hours in glacial acetic acid. The precipitates of the product formed were filtered, washed with ethanol and further purified by recrystallization with DMF and ethanol (1 : 1). The resulting orange-red powder with a melting point ≥ 300 °C was stored in an airtight container at ambient temperature. The structure of the synthesized compound was validated by ^{1}H NMR and ^{13}C NMR spectroscopy (Bruker, 400 MHz, DMSO), as shown in Fig. S1 and S2.†

2.3. Surface modification of (2*Z*,5*Z*)-3-acetyl-2-((3,4-dimethylphenyl)imino)-5-(2-oxoindolin-3-ylidene)thiazolidin-4-one with lanthanum-doped copper oxide (La@CuO-DMT)

A La@CuO-DMT nanohybrid was synthesized by ultrasonication of a 1 : 1 mixture of La@CuO (1 mg mL^{-1} in DI water) and DMT (1 mg mL^{-1} in DMF) for 10 minutes. Ultrasonication enhanced the dispersion of assembling host-guest molecules by acoustic cavitation and aided the π–π interactions for stable hybrid formation.[32] Additionally, the acoustic cavitation induced by sonication enhanced the kinetic energies of the molecules, which aided in establishing equilibrium for the 3D orientation of DMT. The ultrasonication also induced electrostatic interactions between the embodied materials to develop nanohybrids with optimized electronic properties. Meanwhile, without ultrasonication, there will be fewer chances of electrostatic interactions and nanohybrid formation, as we

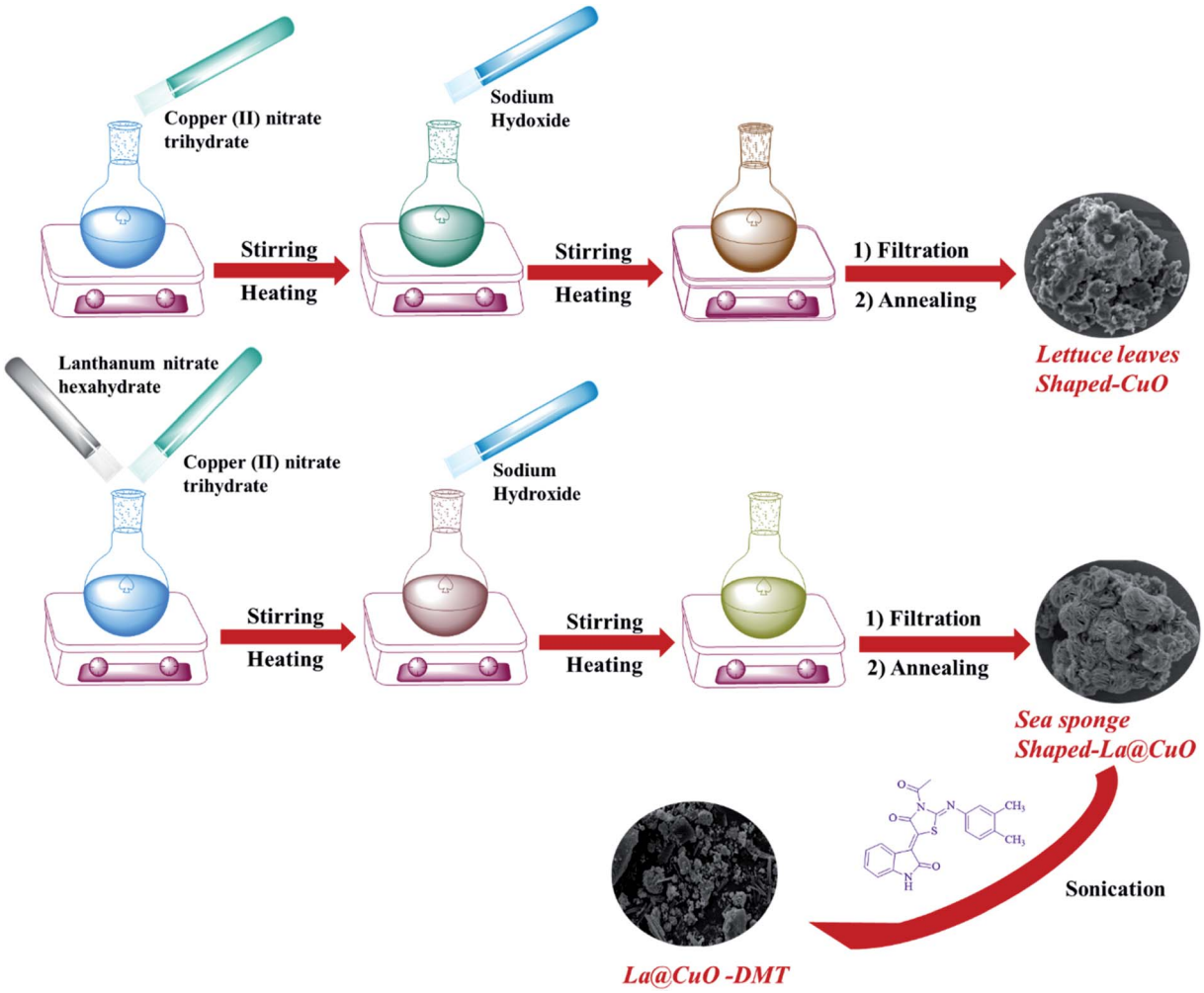

Scheme 1 Schematic illustration of the roadmap implemented for the synthesis of CuO, La@CuO and La@CuO-DMT.

do not have enough kinetic energy. In addition, our slurry does not peel off due to good electrostatic interactions between the GPE and nanohybrids. An ultrasonic bath (100 W, 20 kHz) with 75% DI water at room temperature was employed.

2.4. Electrode fabrication for electrochemical studies

The GPE was selected as a working electrode (2 mm) due to its cost-effectiveness, ease of availability, and minimal pre-treatment requirements. Further, the graphitic surface of sp^2 hybridized carbon provides good adsorption and easy fabrication without using any binder. The synthesized CuO, La@CuO and La@CuO-DMT were used to fabricate the GPE for DA sensing. Before fabrication, the edge of the GPE was cut with the cutter to obtain a smooth and clean working interface followed by washing with DI water. Typically, 2 μL of the synthesized materials were drop-casted to modify the working interface of the GPE and dried at room temperature. This fabricated GPE was moved into an electrochemical cell system and analyzed against DA. Meanwhile, the La@CuO-DMT/GPE interface was also examined under different DA concentrations in phosphate-buffered saline (PBS) by differential pulse voltammetry (DPV) in the potential range of 0–0.8 V with a step size of 25 mV and a pulse size of 250 mV. The same study was executed *via* amperometry by adding DA spikes into a PBS-containing electrochemical cell every 50 s. All the electrochemical experiments were performed at a scan rate of 100 mV s^{-1}.

3. Results and discussion

The SEM images of CuO, La@CuO and La@CuO-DMT are displayed in Fig. 1. CuO exhibits a 3D lettuce leaf-like morphology with an average width of ~2.52 μm, as shown in Fig. 1(A) and (B). However, as the rare earth element (La) was doped, this limited the growth of CuO infrastructures to acquire different nanostructure morphologies with decreased size.[33] Therefore, La@CuO displayed a hierarchal sea sponge-like morphology, as shown in Fig. 1(C). The SEM micrographs further revealed that these sea sponges have evenly distributed and closely packed fine vesicles with an average width of ~0.18 μm, as shown in Fig. 1(D). These fine vesicles containing developed hierarchal sea sponge morphology improved the catalytic characteristics of CuO and aided the robust electron-ion shuttling at the electrode

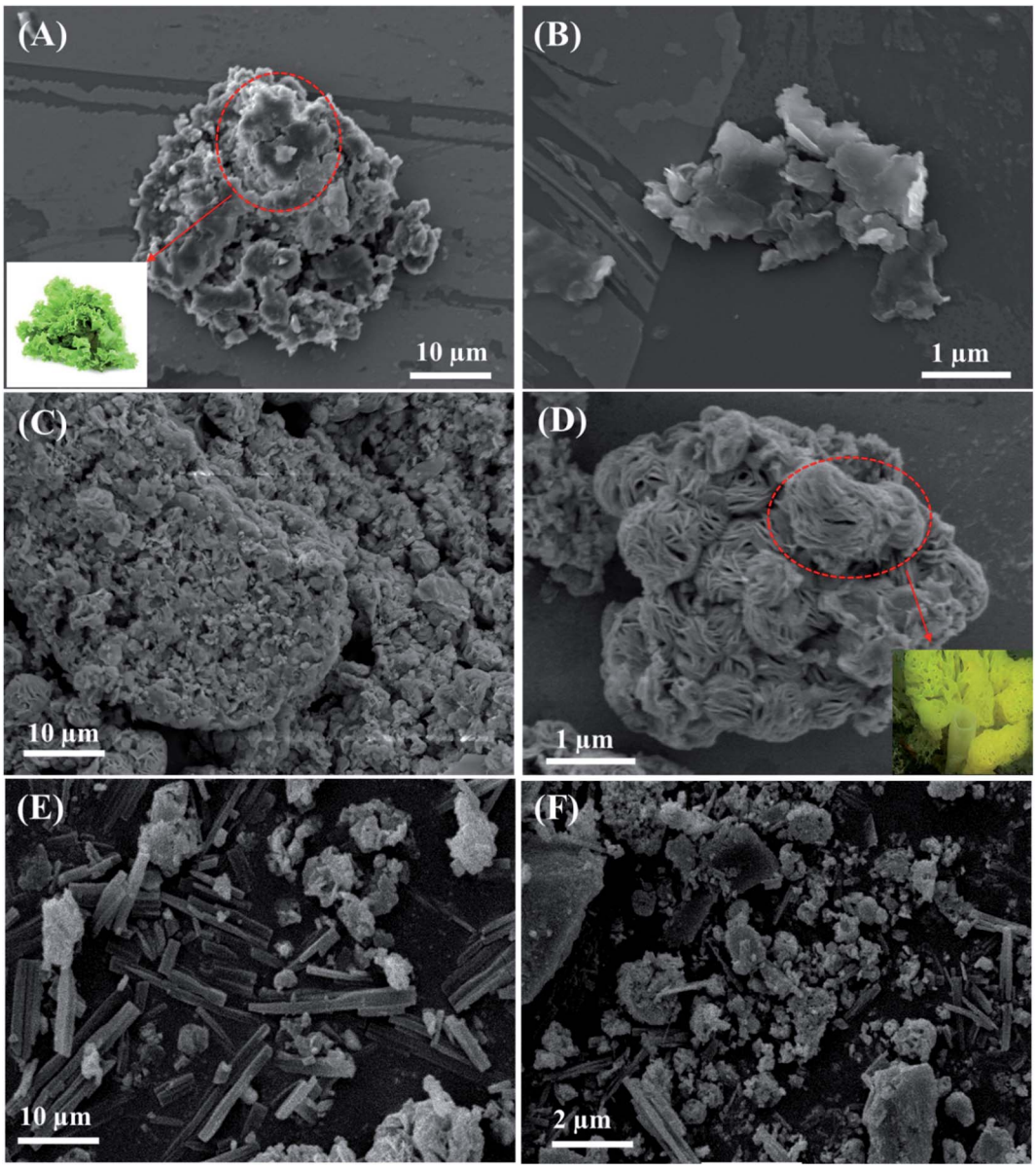

Fig. 1 Scanning electron microscopic images of CuO (A and B), La@CuO (C and D) and La@CuO-DMT (E and F). The inset shows the digital images of lettuce leaves and sea sponge respectively.

interface for DA detection. However, Fig. 1(E) and (F) reveal the distribution of La@CuO in the DMT network.

The XRD patterns of CuO, La@CuO and La@CuO modified DMT are shown in Fig. S3.† The peaks (110), (−111), (111), (−202), (020), (202), (−113) and (022) at 2θ values of 32.4°, 36.3°, 38.6°, 42.2°, 48.7°, 59.2°, 61.3° and 66.1° respectively, correspond to the monoclinic phase structure of CuO,[34] as shown in Fig. S3(a).† However, a corresponding shift in peak positions was observed as a function of annealing temperature after La doping, as shown in Fig. S3(b).† Meanwhile, the peak broadening could be attributed to the induced defects caused by the moderately larger size of lanthanum ions (La = 1.03 Å) compared to copper ions (La = 0.73 Å).[35] Similarly, the change in the intensity and peak position reveals that doping affects the *d* spacing, lattice parameter and crystal quality.[36] However, Bragg's reflection (400) and (411) at 2θ of 30.6° and 33.7° correspond to the cubic La_2O_3 phase (JCPDS card no. 65-3185), as indicated by (◆). All the peaks in doped and undoped CuO are well consistent with the results reported in the literature. However, the diffraction peaks were downshifted in La@CuO-DMT, as revealed in Fig. S3(c).† This shift in scanning angle is attributed to good intercalations between La@CuO and DMT. The remaining prominent diffraction peaks from 11.94 to 26.22 correspond to carbon of the organic DMT molecule.

Raman spectroscopy was implemented to inspect the effect of the introduction of graphitic sp^2 hybridized carbon from DMT and the structural defects created due to La doping in CuO, which influence the surface activity of the designed interface. Two bands originating at 1365 and 1576 cm^{-1} were attributed to the D and G bands for copper oxide

correspondingly, as presented in Fig. S4A(a).† Meanwhile, the bands at 288, 395, and 626 cm^{-1} were due to the Raman active modes A_g, B_{1g} and B_{2g} of copper oxide. However, a minor peak shift in doped CuO could be attributed to the phonon confinement effect.[33] Besides these three vibrational Raman active modes, a multiphonon band of La-doped CuO was observed at 1144 cm^{-1} owing to the higher local density of anisotropic carriers that lead to phonon–plasmon coupling.[37] The I_D/I_G ratio for La@CuO was found to be 0.14. We believed that this I_D/I_G is due to the La addition in the CuO lattice inducing massive structural defects. However, I_D/I_G was shifted to 0.2 after immobilization of La@CuO into the DMT interface. Meanwhile, a significant shift in D and G bands was also observed, signifying the stability of the designed interface owing to good intercalation between embodied materials, as shown in Fig. S4A(b).† These verdicts also revealed that DMT works as an electron transport mediator owing to the presence of a heteroatom (O, N, and S)-rich aromatic skeleton, whereas La@CuO acts as an electrocatalyst.

3.1. Electrocatalytic performance of the integrated interfaces

The electrocatalytic performance of designed electrodes was explored through CV and EIS in 5 mM $[Fe(CN)_6]^{4-/3-}$ as a redox probe to evaluate the electrochemical response, as revealed in Fig. 2. The peak-to-peak separation (ΔE_p) of a bare GPE electrode was found to be much higher (0.28 V), due to the smooth electrode interface. A decrease in ΔE_p (0.18 V) was observed after fabrication with CuO, indicating an increased electrode active surface area and improved morphology,[38] as exposed in Fig. 2A(b). Nevertheless, after fabrication of the GPE with La@CuO, a decrease in ΔE_p (0.13 V) was noticed, as shown in Fig. 2A(c). This improved performance was due to the distribution of different cations caused by the addition of La into the CuO matrix forming La–Cu–O.[39] Thus, La doping induced massive active sites, resulting in enhanced conductivity of the interface. However, a substantial increase in ΔE_p (0.21 V) was witnessed after hybridization with DMT. This anomalous response might be due to the little repulsion between electron-deficient groups equipped with an organic moiety and a $[Fe(CN)_6]^{3-/4-}$ redox probe. Moreover, the anodic peak currents of La@CuO-DMT (162.3 μA) were much higher than its counterparts, *i.e.* bare (28.3 μA), CuO (47.4 μA), and La@CuO (67.7 μA). The higher current suggested the development of a highly stable interface for higher catalytic activity, as observed from Fig. 2A(d). The electrochemical active surface areas (ECSAs) of the designed electrodes were calculated using the Randles–Sevcik equation as follows:[40]

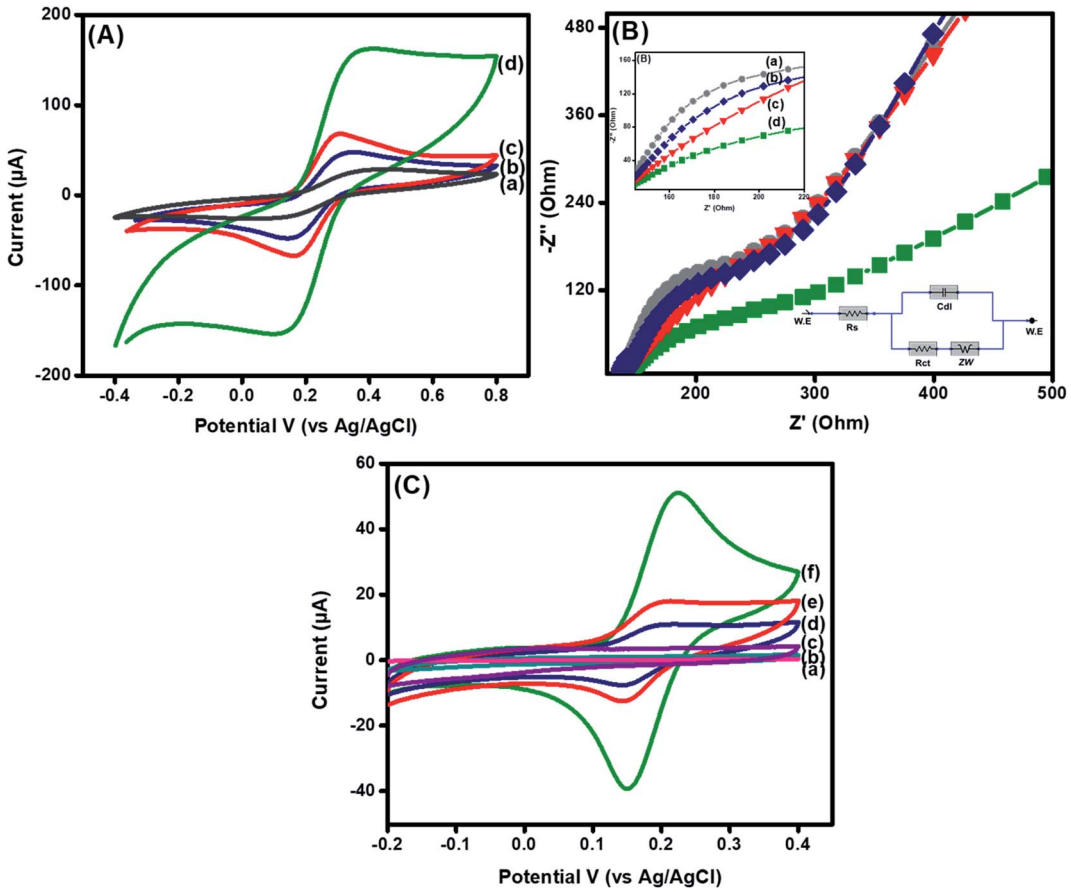

Fig. 2 CV (A) and EIS spectra (B) of (a) bare, (b) CuO, (c) La@CuO, (d) La@CuO/DMT-modified GPE in 5 mM $[Fe(CN)_6]^{4-/3-}$ (1 : 1). CV (C) of (a) CuO, (b) La@CuO, and (c) La@CuO/DMT-modified GPE in PBS and (d) CuO, (e) La@CuO, and (f) La@CuO/DMT in 100 μM dopamine in PBS (pH = 7.4). All the experiments were conducted at a scan rate 100 mV s^{-1}.

$$I_p = 2.69 \times 10^5 A n^{3/2} D_{red}{}^{1/2} C^* \nu^{1/2} \quad (1)$$

where I_p, D_{red}, and A correspond to the anodic peak current, diffusion coefficient of potassium ferrocyanide (7.6×10^{-6} cm^2 s^{-1}) and electrochemical active surface area. While, ν, C and n represent the scan rate (100×10^{-3} V), concentration of ferrocyanide (5×10^{-3} M) and number of electrons involved in the oxidation or reduction of potassium ferro/ferricyanide, which is 1 respectively. The ECSA was found to be 0.03, 0.04, 0.06 and 0.14 cm^2 for bare, CuO, La@CuO and La@CuO-DMT, respectively. The hierarchal hybrid offered fast electron tunneling across the interphase owing to the availability of the greater active surface area resulting in the enhanced electrocatalytic performance.

The electron transfer shuttling and surface charge resistance were further confirmed *via* EIS experiments. The obtained semicircle diameter at higher frequencies in the Nyquist plots corresponds to the electron transfer resistance (R_{et}) and linear portions at a lower frequency parallel to the diffusion-limited mechanism, respectively.[41] The resistance of the bare GPE electrode $R_{ct} = 228\ \Omega$ (Fig. 2B(a)) decreased to $R_{ct} = 146\ \Omega$ after fabrication with CuO (Fig. 2B(b)). This decrease in resistance was due to metal oxide that facilitates the electron transfer.[13] However, a large decrease in resistance ($R_{ct} = 105\ \Omega$) was observed after La doping, as presented in Fig. 2B(c). These results indicated that doping enhanced the electron transfer by exposing catalytically active sites to the redox probe.[22] Furthermore, La@CuO-DMT depicted an increase in charge transfer resistance ($R_{ct} = 214\ \Omega$), as shown in Fig. 2B(d). Additionally, the appearance of a lower frequency line at lower than 45° is attributed to the introduction of large particle-sized DMT molecules that decreased ion transport and increased Warburg resistance leading to a diffusion-limited process.[42]

We further explored the electrochemical behavior of the synthesized materials toward PBS and no peaks were obtained, as shown in Fig. 2C(a–c). Further, we employed the synthesized materials against 100 μM DA in PBS in the potential range of −0.2 V to 0.4 V, as shown in Fig. 2(C). All the modified electrodes showed reversible oxidation upon interaction with analyte DA. These clear redox peaks shown in Fig. 2 are due to the presence of highly electroactive CuOOH layers acting as electrocatalysts in each case, which upon interaction with DA themselves reduce to $Cu(OH)_2$ with (2+) and oxidize DA to dopamine-*O*-quinone. The CuO showed a low peak current (10.8 μA) and a high peak potential (0.23 V) Fig. 2C(a) compared to La@CuO with a peak potential of 0.22 V, as shown in Fig. 2C(b). The increase in faradaic current (17.4 μA) and the decrease in peak potential were due to the surface-induced defects and enhanced surface area after La doping. Meanwhile, the presence of fine vesicles along the whole surface of sea sponge-shaped La@CuO also contributed to enhanced electroactivity, as can be evidenced in SEM images (Fig. 1(C) and (D)). However, the immobilization of La@CuO onto the DMT interface resulted in a maximum faradaic response (50.9 μA) at a decreased detection potential (0.21 V), as shown in Fig. 2C(c). This ideal response could be due to good stability achieved by the conducive DMT support provided for the homogenous immobilization of La@CuO to obtain a highly sensitive sensing interface.

Zeta potential was employed to examine the stability of synthesized materials. The average value of zeta potential for CuO was found to be −12.2 mV signifying the good stability, as shown in Fig. S5(A).† The negative value represented the formation of hydroxyl groups on the CuO surface upon interaction with water.[43] This negative diffused layer of surface OH^- contributes to robust sensing of positively charged DA. However, the zeta potential shifts to −6.3 mV in La@CuO, as shown in Fig. S5(B).† This shift was due to La doping at CuO sites that enhance the stability of CuO.

3.2. Reaction kinetics and mechanistic investigation at developed La@CuO-DMT electrodes

Moreover, CV was performed in 80 μM DA at a scan rate of 25 mV s^{-1} to 400 mV s^{-1} to examine the reaction kinetics and surface activity at the integrated electrode. A positive potential shift in potential was perceived in the CV spectra at an increasing scan rate, as presented in Fig. 3(A). A linear relation was obtained for DA by drawing a graph between anodic peak currents *vs.* scan rates, as shown in Fig. 3(B) and eqn (S4).†

From the slope of the value of Fig. S6(C),† the Tafel slope (b) was calculated using eqn (2) and found to be 0.21 V.[44]

$$E_P = \frac{b}{2} \log \nu + \text{constant} \quad (2)$$

The value of α was premeditated from eqn (3) and found to be 0.03.[45,46]

$$y = 2.303\left(\frac{RT}{\alpha n F}\right) \quad (3)$$

whereas R represents the general gas constant, while T, α, F and n correspond to the absolute temperature, electron transfer coefficient, Faraday constant, and number of electrons transferred. Similarly, the number of electrons transferred at the surface of La@CuO-DMT was found to be 2.30, suggesting the two-electron and two-proton-coupled mechanism.[47]

Moreover, it can be concluded that the enhancement in peak current as revealed previously in Fig. 2C(f) during electrochemical DA oxidation could be due to the release of two electrons and protons into the conduction band of the sensor substrate, as illustrated in Fig. 4 and eqn (4). Briefly, the surface of the developed La@CuO-DMT is endowed with highly electroactive CuOOH layers acting as electrocatalysts owing to the availability of fine vesicles and massive surface defects with fast electron shuttling capability. Meanwhile, La doping in the electroactive layer induced massive active sites that aid in maximum analyte adsorption and enhance electron transfer kinetics, thus amplifying the faradaic response. Meanwhile, the O-, N- and S-awarded DMT boosts the movement of ions and acts as an electron transport booster or mediator. Thus, the catalytically active layer CuOOH upon interaction with DA causes robust and smooth oxidation to dopamine-*O*-quinone and itself reduces to $Cu(OH)_2$ with (2+),[17,48,49] as shown in Fig. 4.

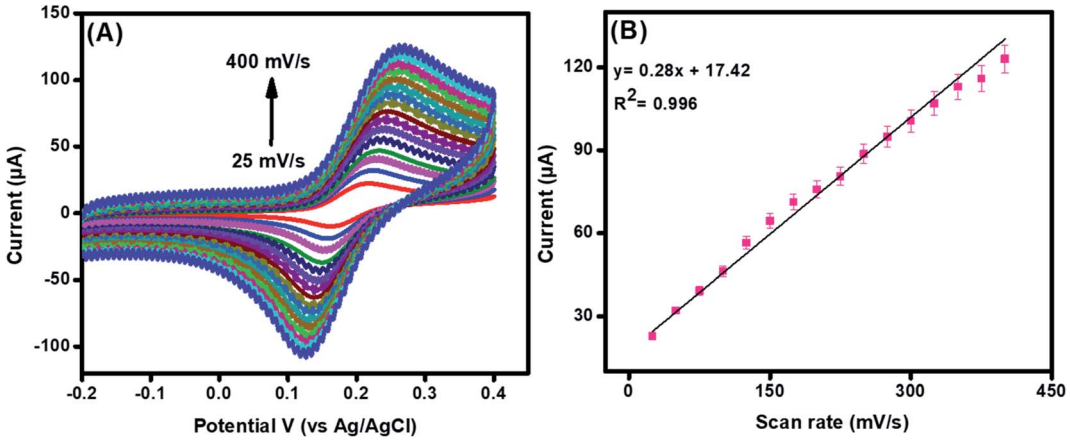

Fig. 3 CV (A) of La@CuO-DMT-modified GPE towards 100 μM DA at different scan rates (25 to 400 mV s^{-1}). Graphs (B) reveal a linear relationship between anodic peak current and scan rate.

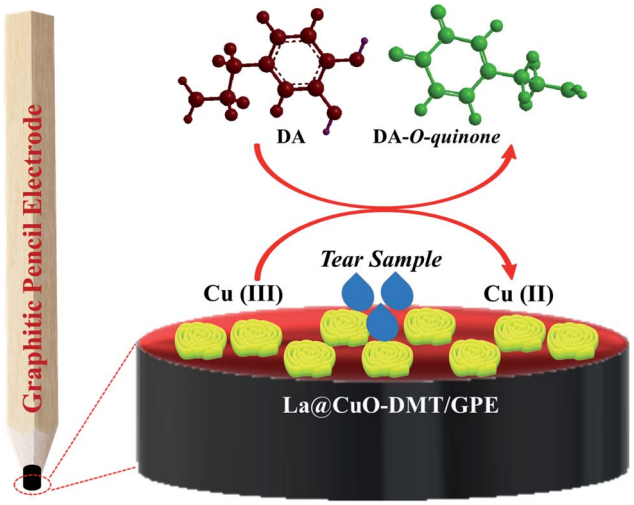

Fig. 4 Sea sponge-shaped La@CuO-decorated O-, N-, and S-rich DMT-wrapped GPE for DA detection.

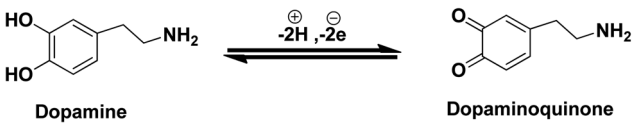

(4)

Besides, we calculated the electron transfer rate constant (K_s) from Laviron equation (5) and, the value was found to be 0.95 s^{-1}.[50,51]

$$\log K_s = \alpha \log(1-\alpha) + (1-\alpha)\log \alpha - \log\left(\frac{RT}{nFv}\right) - \alpha(1-\alpha)nF\Delta E_P/2.3RT \quad (5)$$

3.3. Sensing efficacy of the developed La@CuO and La@CuO-DMT electrodes

We used differential pulse voltammetry (DPV) to observe the response of the designed sensing interface fabricated using La@CuO-DMT against different concentrations of DA owing to its well-defined current response, magnified resolution and capability to decrease non-faradic response.[52] The DPV graphs, as shown in Fig. 5(A) and (B), suggested a linear relationship between faradaic current with the increase in DA concentration. Besides an increase in current, a potential shift was observed in the DPV graph with the increase in DA concentration, proposing the enhanced surface adsorption or coverage of DA at the electrode interface.[53–55]

In addition, we exploited the current sensitive amperometry as well, owing to its capability to achieve a lower detection limit with reduced non-faradic response. The amperometric response of the GPE electrode fabricated using La@CuO and La@CuO-DMT in the linear range of 10–1500 μM of DA in the PBS was obtained at applied potentials of 0.22 V and 0.21 V, respectively, as shown in Fig. 5(C). The robust increase in current upon DA spiking with a response time of 3 s corroborated the high sensing capability of developed electrodes (La@CuO-DMT/GPE). A linear increase in faradaic current was also observed with the increase in DA concentrations, as shown in Fig. 5(D). However, 2 linearity were obtained as revealed in linear graphs of DPV and amperometry. A decreased sensitivity at higher concentrations might be related to the saturation of the electrode surface with the adsorption of DA, *i.e.* electrode fouling that blocks the further adsorption mechanism. Meanwhile, the ohmic drop is a result of the ohmic resistance between the reference and working electrodes, which is also affected by the solution resistance.

The detection limit (LOD) was estimated using the standard method, as shown in eqn (S2)† and found to be 21 nM (S/N = 3) for the integrated La@CuO-DMT/GPE interface. Similarly, the sensitivity was found to be 13.9 μA μM^{-1} cm^{-2}. Interestingly, these results are in good competition with those previously reported in the literature, as displayed in Table S2.† The good sensing efficacy of the integrated interface could be due to the following reasons.

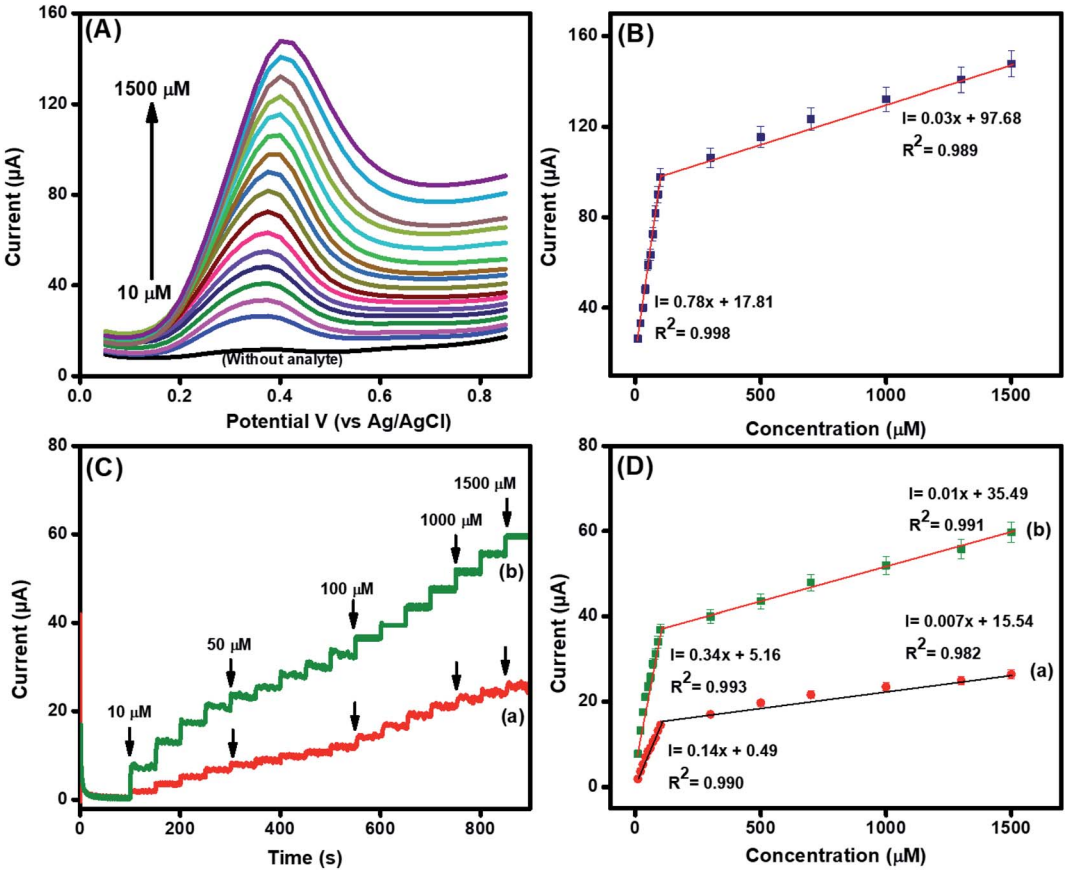

Fig. 5 Differential pulse voltammetry (A) with its corresponding graph (B) and amperometry (C) with its corresponding linear graph (D) for (a) La@CuO and (b) La@CuO-DMT in the concentration range of 10 μM to 1500 μM in phosphate buffer (pH 7.4) at a scan rate of 100 mV s^{-1}.

(1) The presence of a surface hydroxyl layer on CuO enhanced the adsorption of positively charged DA and increased the electron transportation kinetics.

(2) The La doping induced enormous surface defects that offer smooth and robust tunneling of ions at the electrode–electrolyte interface.

(3) The O-, N- and S-enriched DMT moiety acted as a resilient and conducive carbon support and also as an electron booster/mediator to provide high-density π-electrons owing to the presence of the aromatic ring.

3.4. Selectivity, repeatability, reproducibility and stability of integrated sensors

The major challenge associated with the electrochemical sensor development is to selectively analyze the analyte of interest (DA) in the complex biological and physiological media containing coexisting interfering species with parallel oxidizing potentials. Therefore, we inspected the selective efficiency of the integrated La@CuO-DMT/GPE interfaces towards DA. The good amperometric current response of this transducing interface towards DA at an applied potential of 0.21 V could be evidenced in Fig. 6(A). However, the very less or insignificant current response was observed after the addition of interfering analytes such as glucose, cysteine, fructose, and urea even at much higher concentrations (100 μM). This noteworthy selective and specific response might be due to the higher electronegativity of oxygen that inhibits complexation with these analytes. The performance of the integrated sensor was not even affected by ascorbic and uric acid, which are electrocatalytic analogs of DA. This significant behavior is due to the negative charge on ascorbic and uric acid at pH 7.4. Therefore, these interferents are repelled by negatively charged surface hydroxyls on an integrated sensing interface, while DA is charged positively.

The repeatability, reproducibility, and stability of the developed sensing interface were also examined and endorsed under the parallel working parameters. The relative standard deviation (RSD) was found to be 1.15% after repeated usage of the same electrode ($n = 10$), suggesting the good repeatability of the integrated sensor, as shown in Fig. 6(B). The reproducibility of the assimilated sensor was also examined by comparing the 8 electrodes under comparable conditions, as revealed in Fig. 6(C). The RSD, in this case, was found to be 1.07%.

Stability is the primary challenge for sensor development. Therefore, the storage stability of the designed sensing interface

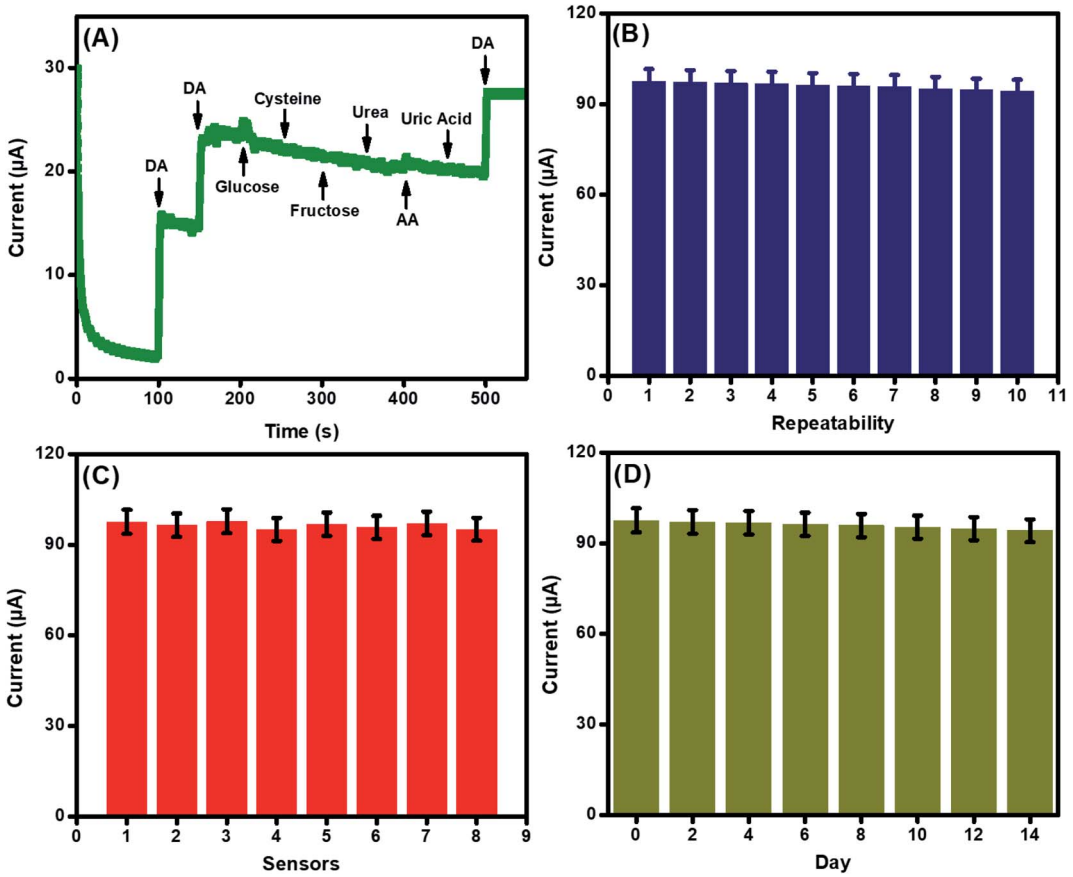

Fig. 6 Current response (A) of La@CuO-DMT in the presence of 20 μM DA (first 2 spikes), 30 μM DA (last spike) and 100 μM interfering species in PBS (pH 7.4) at a scan rate of 100 mV s^{-1}. Repeatability (B) of La@CuO-DMT of the fabricated electrodes for their response towards DA ten times. Reproducibility (C) of La@CuO-DMT of 6 fabricated electrodes for their response towards DA in an analogous environment. Stability (D) of La@CuO-DMT of the fabricated electrode and its response towards DA were analyzed after every 7 days for 14 days.

was also studied, as shown in Fig. 6(D). The primed sensors were stored at room temperature and were examined after every 2 days for 14 days. The RSD was calculated to be 1.20% in this case, which demonstrated the long-term shelf life of the designed sensing system.

3.5. Real sample analysis on the designed La@CuO-DMT/GPE interface

The practical development of electrochemical sensing interfaces is a big challenge, as real samples contain many interfering biological species other than target analytes. Therefore, real sample analysis was performed on the as-developed sensing interface to practically analyze the analytical performance. The recovery data of DA at four different spiked concentrations (20 μM, 50 μM, 100 μM and 300 μM) in PBS (pH 7.4) are revealed in Table S1.† The assay protocol is described in detail in ESI.†[56,57] The recoveries were premeditated using eqn (S1)† and found to be in the range of 99.1 to 100.1%, as shown in Table S1.† Moreover, to examine the selectivity traits of the assimilated electrochemical sensor, the standard addition method was applied to the tear samples. These good recovery data of the DA spiked tear samples endorse the high sensing efficacy in complex media.

4. Conclusions

In this work, a novel DMT has been synthesized for the fabrication of La@CuO to selectively monitor DA. The designed interface allows for the sensitive and robust monitoring of DA in the presence of interfering analytes with considerable reproducibility. The sea sponge-shaped La@CuO nanoparticles offer exposed catalytically active sites with a defined morphology to increase analyte adsorption and enhance reaction kinetics, leading to an amplified faradaic response. Additionally, the presence of O-, N-, and S-rich high-concentration graphitic layers offers fast shuttling of electrons and ions at the electrode–electrolyte interface, leading to a decreased detection limit. The designed sensor was effectively employed to detect DA from tear samples, thus signifying the practical reliability of the designed interface. To the best of our knowledge, our developed sensor displayed novelty not only in composition but in the application too.

Conflicts of interest

The authors declare that they have no known competing financial interests or personal relationships that could have appeared to influence the work reported in this paper.

Acknowledgements

UA acknowledges the financial support provided by HEC under the indigenous Ph.D. 5000 fellowship program (2PS5-179/HEC/IS/2019) to pursue her Ph.D. at BZU Multan. MHN acknowledges the financial support provided by HEC (20-4993/R&D/HEC/14/614) and CUI (16-14/CRGP/CIIT/LHR/15/776).

References

1 F. Sun, J. Zhou, B. Dai, T. Qian, J. Zeng, X. Li, Y. Zhuo, Y. Zhang, Y. Wang and C. Qian, *Nat. Methods*, 2020, **17**, 1156–1166.
2 C. Liu, P. Goel and P. S. Kaeser, *Nat. Rev. Neurosci.*, 2021, 1–14.
3 A. A. Grace, *Nat. Rev. Neurosci.*, 2016, **17**, 524.
4 H. Y. Y. Nyein, M. Bariya, B. Tran, C. H. Ahn, B. J. Brown, W. Ji, N. Davis and A. Javey, *Nat. Commun.*, 2021, **12**, 1–13.
5 F. Gao, J. Song, Z. Xu, L. Xu, Y. Guo, L. Miao and X. Luo, *Sens. Actuators, B*, 2021, **334**, 129675.
6 T. Kokulnathan, F. Ahmed, S.-M. Chen, T.-W. Chen, P. Hasan, A. L. Bilgrami and R. Darwesh, *ACS Appl. Mater. Interfaces*, 2021, **13**, 10987–10995.
7 Q. He, J. Liu, X. Liu, G. Li, D. Chen, P. Deng and J. Liang, *Electrochim. Acta*, 2019, **296**, 683–692.
8 A. Vázquez-Guardado, S. Barkam, M. Peppler, A. Biswas, W. Dennis, S. Das, S. Seal and D. Chanda, *Nano Lett.*, 2018, **19**, 449–454.
9 Q. Li, Y. Xia, X. Wan, S. Yang, Z. Cai, Y. Ye and G. Li, *Mater. Sci. Eng., C*, 2020, **109**, 110615.
10 A. Padmanaban, N. Padmanathan, T. Dhanasekaran, R. Manigandan, S. Srinandhini, P. Sivaprakash, S. Arumugam and V. Narayanan, *J. Electroanal. Chem.*, 2020, **877**, 114658.
11 L. Wei, J. Ding, J. Wu, L. Li, Q. Li, L.-X. Shao, J. Lu and J. Qian, *Talanta*, 2022, 123263.
12 L. Wei, J. Ding, L. Shao, J. Lu and J. Qian, *Mater. Lett.*, 2021, **295**, 129839.
13 B. Liu, X. Ouyang, Y. Ding, L. Luo, D. Xu and Y. Ning, *Talanta*, 2016, **146**, 114–121.
14 R. A. Soomro, K. R. Hallam, Z. H. Ibupoto, A. Tahira, S. Jawaid, S. T. H. Sherazi and M. Willander, *RSC Adv.*, 2015, **5**, 105090–105097.
15 N. Verma and N. Kumar, *ACS Biomater. Sci. Eng.*, 2019, **5**, 1170–1188.
16 K. Krishnamoorthy, V. Sudha, S. M. S. Kumar and R. Thangamuthu, *J. Alloys Compd.*, 2018, **748**, 338–347.
17 S. Sundar, G. Venkatachalam and S. J. Kwon, *Nanomaterials*, 2018, **8**, 823.
18 L. Zhang and H. Wang, *ACS Nano*, 2011, **5**, 3257–3267.
19 L. Dörner, C. Cancellieri, B. Rheingans, M. Walter, R. Kägi, P. Schmutz, M. V. Kovalenko and L. P. Jeurgens, *Sci. Rep.*, 2019, **9**, 1–13.
20 N. Tammanoon, A. Wisitsoraat, D. Phokharatkul, A. Tuantranont, S. Phanichphant, V. Yordsri and C. Liewhiran, *Sens. Actuators, B*, 2018, **262**, 245–262.
21 J. D. Rodney, S. Deepapriya, M. C. Robinson, C. J. Raj, S. Perumal, B. C. Kim and S. J. Das, *Int. J. Hydrogen Energy*, 2020, **45**, 24684–24696.
22 M. M. Foroughi, S. Jahani and H. H. Nadiki, *Sens. Actuators, B*, 2019, **285**, 562–570.
23 A. A. Pathan, K. R. Desai and C. Bhasin, *Int. J. Nanomater. Chem.*, 2017, **3**, 21–25.
24 J. Ding, L. Zhong, X. Wang, L. Chai, Y. Wang, M. Jiang, T.-T. Li, Y. Hu, J. Qian and S. Huang, *Sens. Actuators, B*, 2020, **306**, 127551.
25 Z. Song, W. Liu, N. Sun, W. Wei, Z. Zhang, H. Liu, G. Liu and Z. Zhao, *Solid State Commun.*, 2019, **287**, 27–30.
26 A. Mohammadi, Z. Dehghan, M. Rassa and N. Chaibakhsh, *Sens. Actuators, B*, 2016, **230**, 388–397.
27 S. G. Hammad, M. G. El-Gazzar, N. S. Abutaleb, D. Li, I. Ramming, A. Shekhar, M. Abdel-Halim, E. Z. Elrazaz, M. N. Seleem and U. Bilitewski, *Bioorg. Chem.*, 2020, **95**, 103517.
28 R. Singh, M. R. Saini, D. Bhardwaj and A. Singh, *New J. Chem.*, 2020, **44**, 7923–7931.
29 D. Akram, I. A. Elhaty and S. S. AlNeyadi, *Chemosensors*, 2020, **8**, 16.
30 R. Diana, U. Caruso, S. Concilio, S. Piotto, A. Tuzi and B. Panunzi, *Dyes Pigm.*, 2018, **155**, 249–257.
31 M. El-Naggar, W. M. Eldehna, H. Almahli, A. Elgez, M. Fares, M. M. Elaasser and H. A. Abdel-Aziz, *Molecules*, 2018, **23**, 1420.
32 S. Riaz, W. Feng, A. F. Khan and M. H. Nawaz, *J. Appl. Polym. Sci.*, 2016, **133**, 24.
33 J. D. Rodney, S. Deepapriya, P. A. Vinosha, S. Krishnan, S. J. Priscilla, R. Daniel and S. J. Das, *Optik*, 2018, **161**, 204–216.
34 H. Khmissi, A. El Sayed and M. Shaban, *J. Mater. Sci.*, 2016, **51**, 5924–5938.
35 L. V. Devi, T. Selvalakshmi, S. Sellaiyan, A. Uedono, K. Sivaji and S. Sankar, *J. Alloys Compd.*, 2017, **709**, 496–504.
36 L. V. Devi, S. Sellaiyan, S. Sankar and K. Sivaji, *Mater. Res. Express*, 2018, **5**, 024002.
37 W. Wang, Q. Zhou, X. Fei, Y. He, P. Zhang, G. Zhang, L. Peng and W. Xie, *CrystEngComm*, 2010, **12**, 2232–2237.
38 C. Punckt, M. A. Pope and I. A. Aksay, *J. Phys. Chem. C*, 2013, **117**, 16076–16086.
39 M. Rajaei, M. M. Foroughi, S. Jahani, M. S. Zandi and H. H. Nadiki, *J. Mol. Liq.*, 2019, **284**, 462–472.
40 U. Amara, K. Mahmood, S. Riaz, M. Nasir, A. Hayat, M. Hanif, M. Yaqub, D. Han, L. Niu and M. H. Nawaz, *Microchem. J.*, 2021, 106109.
41 S. Rashid, M. H. Nawaz, I. ur Rehman, A. Hayat and J. L. Marty, *Sens. Actuators, B*, 2021, **330**, 129351.
42 P. Leuaa, D. Priyadarshani, A. K. Tripathi and M. Neergat, *J. Phys. Chem. C*, 2019, **123**, 21440–21447.
43 N. Anandhavalli, B. Mol, S. Manikandan, N. Anusha, V. Ponnusami and K. Rajan, *Asian J. Chem.*, 2015, **27**, 2523–2526.
44 B. Jahanshahi, J. Raoof, M. Amiri-Aref and R. Ojani, *J. Chil. Chem. Soc.*, 2014, **59**, 2692–2696.

45 A. Sukeri, L. P. H. Saravia and M. Bertotti, *Phys. Chem. Chem. Phys.*, 2015, **17**, 28510–28514.
46 U. Amara, K. Mahmood, M. Awais, M. Khalid, M. Nasir, S. Riaz, A. Hayat and M. H. Nawaz, *Dalton Trans.*, 2022, **51**, 5098–5107.
47 T. Kokulnathan, A. J. Anthuvan, S.-M. Chen, V. Chinnuswamy and K. Kadirvelu, *Inorg. Chem. Front.*, 2018, **5**, 705–718.
48 M. Asad, A. Zulfiqar, R. Raza, M. Yang, A. Hayat and N. Akhtar, *Electroanalysis*, 2020, **32**, 11–18.
49 U. Amara, S. Riaz, K. Mahmood, N. Akhtar, M. Nasir, A. Hayat, M. Khalid, M. Yaqub and M. H. Nawaz, *RSC Adv.*, 2021, **11**, 25084–25095.
50 Y. Zhou, W. Tang, J. Wang, G. Zhang, S. Chai, L. Zhang and T. Liu, *Anal. Methods*, 2014, **6**, 3474–3481.
51 U. Amara, B. Sarfraz, K. Mahmood, M. T. Mehran, N. Muhammad, A. Hayat and M. H. Nawaz, *Microchim. Acta*, 2022, **189**, 1–12.
52 L. A. Mercante, A. Pavinatto, L. E. Iwaki, V. P. Scagion, V. Zucolotto, O. N. Oliveira Jr, L. H. Mattoso and D. S. Correa, *ACS Appl. Mater. Interfaces*, 2015, **7**, 4784–4790.
53 S. Reddy, B. K. Swamy and H. Jayadevappa, *Electrochim. Acta*, 2012, **61**, 78–86.
54 C. N. Hobbs, J. A. Johnson, M. D. Verber and R. M. Wightman, *Analyst*, 2017, **142**, 2912–2920.
55 R. Ramachandran, X. Leng, C. Zhao, Z.-X. Xu and F. Wang, *Appl. Mater. Today*, 2020, **18**, 100477.
56 M. L. Yola, *Microchim. Acta*, 2021, **188**, 1–13.
57 C. Karaman, O. Karaman, N. Atar and M. L. Yola, *Microchim. Acta*, 2021, **188**, 1–15.